The Astrophysical Journal, 799:45 (6pp), 2015 January 20 doi:10.1088/0004-637X/799/1/45

THE LOCAL GROUP IN THE COSMIC WEB

J. E. Forero-Romero[1] and R. González[2,3]
[1] Departamento de Física, Universidad de los Andes, Cra. 1 No. 18A-10, Edificio Ip, Bogotá, Colombia; je.forero@uniandes.edu.co
[2] Instituto de Astrofísica, Pontificia Universidad Católica de Chile, Av. Vicuña Mackenna 4860, Santiago, Chile; regonzar@astro.puc.cl
[3] Centro de Astro-Ingeniería, Pontificia Universidad Católica de Chile, Av. Vicuña Mackenna 4860, Santiago, Chile
Received 2014 August 14; accepted 2014 November 10; published 2015 January 14

ABSTRACT

We explore the characteristics of the cosmic web around Local-Group (LG)-like pairs using a cosmological simulation in the ΛCDM cosmology. We use the Hessian of the gravitational potential to classify regions on scales of ∼2 Mpc as a peak, sheet, filament, or void. The sample of LG counterparts is represented by two samples of halo pairs. The first is a general sample composed of pairs with similar masses and isolation criteria as observed for the LG. The second is a subset with additional observed kinematic constraints such as relative pair velocity and separation. We find that the pairs in the LG sample with all constraints are: (1) preferentially located in filaments and sheets, (2) located in a narrow range of local overdensity $0 < \delta < 2$, web ellipticity $0.1 < e < 1.0$, and prolateness $-0.4 < p < 0.4$, (3) strongly aligned with the cosmic web. The alignments are such that the pair orbital angular momentum tends to be perpendicular to the smallest tidal eigenvector, $\hat{e}_3$, which lies along the filament direction or the sheet plane. A stronger alignment is present for the vector linking the two halos with the vector $\hat{e}_3$. Additionally, we fail to find a strong correlation between the spin of each halo in the pair with the cosmic web. All of these trends are expected to a great extent from the selection of LG total mass in the general sample. Applied to the observed LG, there is a potential conflict between the alignments of the different satellite planes and the numerical evidence for satellite accretion along filaments; the direction defined by $\hat{e}_3$. This highlights the relevance of achieving a precise characterization for the location of the LG in the cosmic web in the cosmological context provided by ΛCDM.

Key words: dark matter – Local Group

1. INTRODUCTION

The spatial and kinematic configuration of Local Group (LG) galaxies is very uncommon in the local universe as well as in cosmological simulations. The LG is dominated by two big spirals: the Milky Way (MW) and M31, the next most luminous galaxy is M33, which is ∼10 times less massive than M31, followed by several dozen less luminous dwarf galaxies, up to a distance of ∼3 Mpc. The velocity vector of M31, with a low tangential velocity is consistent with a head-on collision orbit toward the MW (Cox & Loeb 2008; van der Marel et al. 2012b; Sohn et al. 2012).

Another feature of the LG is the relatively low velocity dispersion of nearby galaxies up to ∼8 Mpc (Sandage & Tammann 1975; Aragon-Calvo et al. 2011, and references therein). The environment around the LG has a density that is quite close to the average density of the universe (Klypin et al. 2003; Karachentsev 2005). In addition, the closest massive galaxy cluster, the Virgo Cluster, is ∼16.5 Mpc away (Mei et al. 2007).

In addition, the LG is located in a diffuse and warped filament/wall connecting the Virgo Cluster with the Fornax Cluster, some nearby galaxies and group members of this large structure are the Maffei group, NGC 6744, NGC 5128, M101, M81, NGC 1023, and Cen A (Courtois et al. 2013). At this scale, there is no evident alignment of the MW–M31 orbital plane with any local filament or in the Virgo–Fornax direction. However, if we look at a smaller volume, below scales of ∼6 Mpc, there is a clear alignment of the MW–M31 orbit with a local plane of galaxies as shown by Figure 3 in Courtois et al. (2013). Furthermore, the satellite galaxies in the MW and M31 present different kinds of strong alignments along planes (Pawlowski et al. 2013; Shaya & Tully 2013), which are sometimes considered to be unusual in the context of the Λ cold dark matter (CDM) model (Pawlowski et al. 2012).

This combination of features makes LG analogs uncommon. Using numerical simulations, González et al. (2014) found that less than 2% of MW-sized halos reside in a pair similar to MW–M31 and with similar LG environment. Furthermore, if we select pairs that are constrained within a 2σ error from current observational measurements of the velocity components and distance to M31, then there are only 46 systems in a cubic volume of 250 h^{-1} Mpc side, giving a number density of $\sim 1.0 \times 10^{-6}$ Mpc^3, which is comparable to the abundance of massive clusters. A similar abundance was found by Forero-Romero et al. (2011) by comparing the formation history of LG pairs in constrained simulations with the results of unconstrained cosmological simulations.

Forero-Romero et al. (2013) also studied MW–M31 pairs in numerical simulations, finding that the typical quantities characterizing the orbital parameters of the LG are rare among typical pairs, but not sufficiently rare to challenge the ΛCDM model. Another set of criteria for LG analogs was used by Li & White (2008), but, despite differences in the definitions and resulting fraction of LG analogs, their results are in agreement with the frequency of low pairs as well.

To better understand the properties of the LG and how this uncommon pair configuration can be explained in the cosmological context, some questions arise. What else can we say of the environment of the LG on larger scales? To what extent is this an expected configuration in ΛCDM? In particular, what are the typical/preferred locations of these systems within the cosmic web? Are the preferential alignments of satellites a result of the location of the LG in the cosmic web?

In this paper we address those questions by studying the large-scale environment of LG analogs in the context of ΛCDM.

We use the Bolshoi simulation to explore what structures they reside in and if there is any correlation or alignment with the cosmic web. The large-scale environment is defined by the cosmic web components identified by Forero-Romero et al. (2009), and we use the LG analogs computed by González et al. (2014).

This paper is organized as follows. In Section 2, we present the N-body cosmological simulation and the algorithm to define the cosmic web. Next, in Section 3, we describe the sample of LG analogs extracted from the simulation. In Section 4, we present our results and wrap up with a discussion and conclusions in Section 5.

2. SIMULATION AND WEB FINDING ALGORITHM

2.1. The Bolshoi Simulation

We use the Bolshoi simulation of ΛCDM cosmology: $\Omega_{\rm m} = 1 - \Omega_\Lambda = 0.27$, $H_0 = 70\ {\rm km\,s^{-1}\,Mpc^{-1}}$, $\sigma_8 = 0.82$, $n_s = 0.95$ (Klypin et al. 2011), compatible with the constraints from the *Wilkinson Microwave Anisotropy Probe* satellite (Hinshaw et al. 2013). The simulation followed the evolution of dark matter in a $250\,h^{-1}$ Mpc box with a spatial resolution of $\sim 1\,h^{-1}$ kpc and a mass resolution of $m_{\rm p} = 1.35 \times 10^8\ M_\odot$. Halos are identified with the Bound Density Maxima (BDM) algorithm (Klypin & Holtzman 1997). The BDM algorithm is a spherical overdensity halo finding algorithm and is designed to identify both host halos and subhalos.

2.2. Cosmic Web Identification

The web finding algorithm is based on the tidal tensor computed as the Hessian of the gravitational potential field

$$T_{ij} = \frac{\partial^2 \phi}{\partial r_i \partial r_j}, \tag{1}$$

where r_i, $i = 1, 2, 3$ refers to the three spatial comoving coordinates and ϕ is the gravitational potential renormalized to follow the Poisson equation $\nabla^2\phi = \delta$, where δ is the matter overdensity.

This tensor is real and symmetric, which means that it can be diagonalized. We denote its eigenvalues as $\lambda_1 \geqslant \lambda_2 \geqslant \lambda_3$ and their corresponding eigenvectors $\hat{e}_1$, $\hat{e}_2$, and $\hat{e}_3$. The web classification compares each one of the three eigenvalues to a threshold value $\lambda_{\rm th}$. If the three, two, one, or zero eigenvalues are larger than this threshold, then the region is classified as peak, filament, sheet, or void, respectively. Because this tensor is also known as the tidal tensor, we refer to it as the Tweb algorithm.

Forero-Romero et al. (2009) performed a detailed study for the topology of the cosmic web and its visual counterpart as a function of the parameter $\lambda_{\rm th}$. They found that reasonable results in terms of the volume fraction occupied by voids, the visual inspection, and the halo populations in each web type can be reached by values of $0.2 < \lambda_{\rm th} < 0.4$. In this paper, we choose the value of $\lambda_{\rm th} = 0.3$ to proceed with our analysis. This is only relevant to the classification of the simulation into web elements. Other results are completely independent of this choice. Nevertheless, we have checked that the main conclusions of this work do not depend on the precise choice of $\lambda_{\rm th}$.

The algorithm to compute the potential is grid-based. First, we interpolate the mass into a cubic grid with a Cloud-In-Cell scheme and smooth it with a Gaussian kernel in order to reduce the grid influence in the computations that follow. Then, we obtain the gravitational potential using fast Fourier transform methods and use finite differences to compute the Hessian at every point in the grid. In our case, we have used a grid size and a Gaussian smoothing that are two times larger than the typical separation between the two halos in the LG. The purpose of this choice is to give both halos in the pair a common environment. In this paper, we use a grid spacing of $s = 0.97\ h^{-1}$ Mpc, corresponding to a 256^3 grid in the Bolshoi volume. The scale for the Gaussian smoothing uses the same value.

We use the matter overdensity, ellipticity, and the prolateness to further characterize the web. These quantities are defined in terms of the eigenvalues as follows.

$$\delta = \lambda_1 + \lambda_2 + \lambda_3, \tag{2}$$

$$e = \frac{\lambda_3 - \lambda_1}{2(\lambda_1 + \lambda_2 + \lambda_3)}, \tag{3}$$

$$p = \frac{\lambda_1 + \lambda_3 - 2\lambda_2}{2(\lambda_1 + \lambda_2 + \lambda_3)}. \tag{4}$$

We also measure the alignment of the LG halos with respect to the cosmic web defined by their eigenvectors. To this end, we characterize each LG pair by two vectors. The first is $\hat{n}$, the axis along the orbital angular momentum of the pair, normal to its orbital plane; the second is $\hat{r}$, the vector that connects the halos in the pair that can be related to the alignment of the radial velocities to the web. We quantify the alignment using the absolute value of the cosine of the angle between the two vectors of interest $\mu = |\hat{e}_i \cdot \hat{n}|$ or $\mu = |\hat{e}_i \cdot \hat{r}|$, where $i = 1, 2, 3$.

We have verified that the main trends reported in this paper remain unchanged if we use the results from a 512^3 grid, smoothed over scales of $s = 0.48\ h^{-1}$ Mpc. Small changes of a factor of ∼2 in the smoothing scale do not significantly impact the cosmic web, as it was shown in Forero-Romero et al. (2009) from the study of the volume- and mass-filling fractions for different smoothing scales. Other works have also shown that broad features in the cosmic web, as defined in this paper, are robust to changes that are of factors of ∼2 on the scale defining the web (Cautun et al. 2014).[4]

3. LOCAL GROUP ANALOGS

To construct a sample of the MW–M31 pairs at $z \sim 0$, we use a series of simulation snapshots at $z < 0.1$ (since the last ∼1.3 Gyr) spaced by ∼150–250 Myr. This is done because a particular configuration of MW and M31 is transient and corresponds to a relatively small number of systems at one snapshot. By using multiple snapshots, we can increase the sample of systems in such a configuration during a period of time in which secular cosmological evolution is small.

The LG analogs, or the general sample (GS), in this paper are pairs selected in relative isolation, and in a wide range of masses from $M_{200c} = 5 \times 10^{11}\ M_\odot$ to $5 \times 10^{13}\ M_\odot$. Isolation criteria include pair members closer than 1.3 Mpc with no massive neighbors within 5 Mpc. In addition, we require that pairs have no Virgo-like neighbor halos with masses of $M_{200c} > 1.5 \times 10^{14}\ M_\odot$ within 12 Mpc. We have 5480 pairs under these general criteria. A full description of the selection criteria can be found in González et al. (2013, 2014).

We also define two subsets of restricted samples (RS) more closely related to the MW–M31 dynamics according to the tolerance in additional constraints. A sample named 2σ, corresponding to LG analogs constrained by two times the observational

[4] The data of the BDM halos and the Tweb is publicly available through a database located at http://www.cosmosim.org/. A detailed description of the database structure was presented by Riebe et al. (2013).

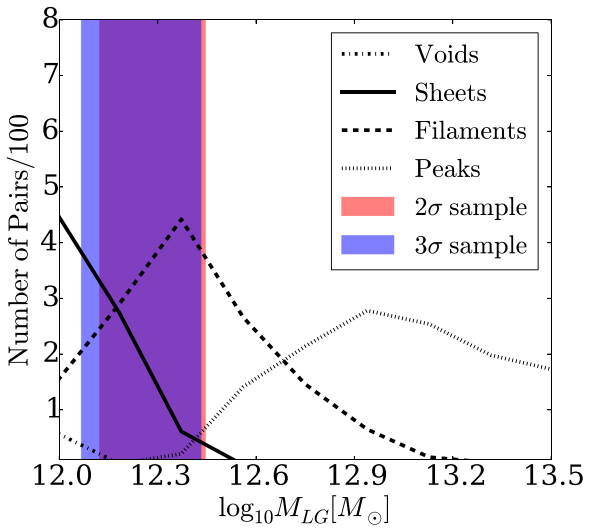

Figure 1. Mass distribution of pairs in different environments for the general sample. The shaded regions show the 68% confidence interval of the mass ranges for 2σ and 3σ samples.

errors in the orbital values (radial velocity, tangential velocity, and separation), and a more relaxed sample named 3σ for LG analogs constrained by three times the observational errors accordingly. The number of pairs in each sample is 46 and 120, respectively; note that we have fewer pairs than in González et al. (2014) since we removed pairs that are too close at $z = 0$, i.e., their virial radii overlap. Also, we removed a couple of pairs that merged or change their mass more than 20% at the present time since they were detected at $z < 0.1$.

4. RESULTS

4.1. The Preferred Environment for LGs

The first result that we explore is the kind of environment occupied by our LGs, and we use it as a reference sample for the GS where pairs are much more relaxed in mass and kinematic constraints. We find that the pairs in the GS are located across all different environments without any strong preferences; one-third are located in sheets, one-fourth are in peaks, one-fourth are in filaments, and the remaining one-sixth are in voids.

The situation in the 2σ and 3σ samples is very different. By and large, the LGs in these samples are located in filaments and sheets. In both samples, ~50% of the pairs can be found in filaments, while ~40% are in sheets. These absolute numbers in each environment for each sample are presented in Table 1.

We find that the difference between the GS and the RS can be explained by the total pair mass. In González et al. (2014), the mass range covered by 2σ and 3σ samples is very narrow and it is used to constraint the LG mass. We show in Table 1 that a subset of the GS that has a similar mass range as the RS reproduces similar environment fractions. The correlation between halo mass and their environment is a well-known result (Lee & Shandarin 1998).

Figure 1 summarizes this correlation between environment an total pair mass. Each line represents the mass distribution of pairs in the four different environments of the GS. High-mass pairs tend to be located in peaks and filaments while less massive ones tend to be in voids and sheets. The shaded regions represent the 68% confidence intervals of the mass distributions of 2σ and 3σ samples.

4.2. Web Overdensity, Ellipticity, and Prolateness

We now characterize the preferred location of the pair samples in terms of the web overdensity, ellipticity, and anisotropy as defined in Section 2.

Figure 2 shows the dependency of these three characteristics on the total pair mass for the different samples. GS is represented by the solid lines with the associated errors covered by the shaded region. The symbols represent the results for the 2σ and 3σ samples. In the three cases, it is evident that the range of values for the 2σ and 3σ samples are completely expected from the mass constraint alone.

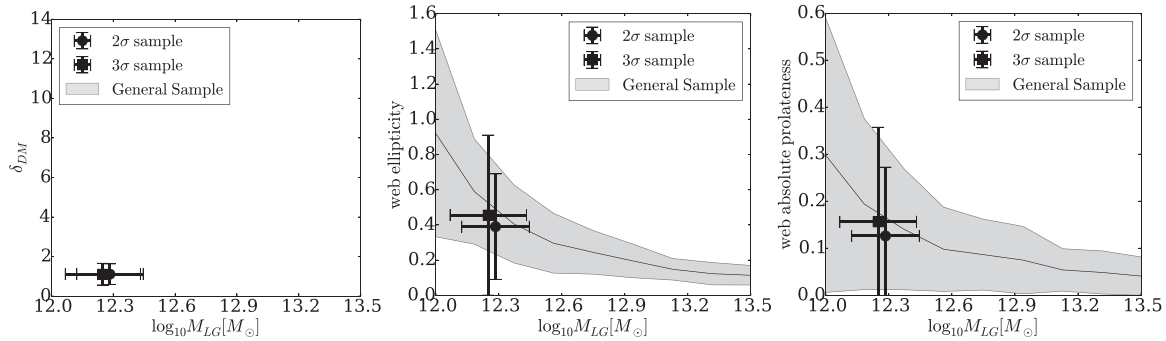

Figure 2. Mass dependency of the average dark matter overdensity (left), web ellipticity (middle), and web absolute value prolateness (right) at the pair location. The shaded contours indicate the 68% confidence region.

Table 1
Number of Pairs in the Four Different Kinds of Environments for Each of the Three Samples Presented in Section 3

Sample	Peak n (%)	Filament n (%)	Sheet n (%)	Void n (%)
2σ	4 (8.7)	24 (52.2)	17 (36.7)	1 (2.2)
3σ	10 (8.3)	58 (48.3)	47 (39.2)	5 (4.2)
General	1312 (23.9)	1472 (26.9)	1769 (32.3)	927 (16.9)
General ($12.1 < \log_{10} M_{\rm LG}/M_\odot < 12.3$)	8 (1.4)	334 (55.5)	259 (43.0)	1 (0.1)

Notes. In parenthesis is the same number, but as a percentage of the total population. The last line in the table corresponds to the general sample with an additional mass cut for the total pair mass.

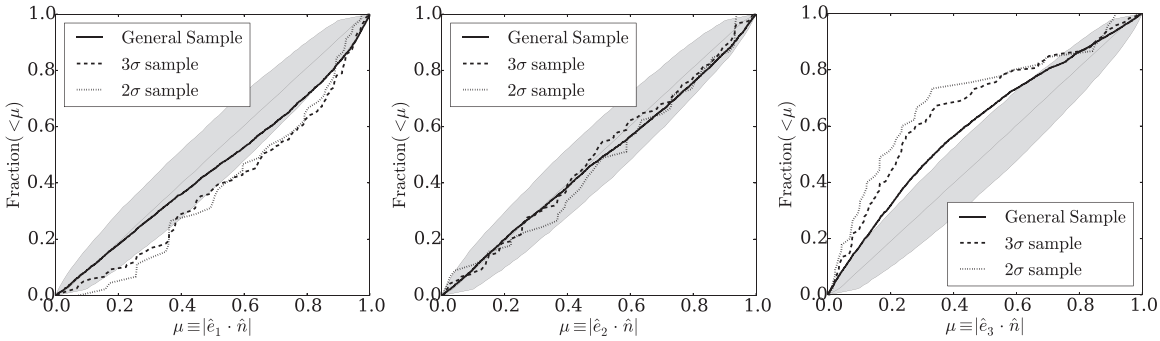

Figure 3. Cumulative distributions for the alignment between the normal vector to the pair orbital plane, $\hat{n}$, and the three eigenvectors in the Tweb. The shaded region shows the expectation for a random distribution without any preferential alignment, it encloses the 5% and 95% percentiles of 10,000 flat distributions for μ generated with the same number of points as the 2σ sample.

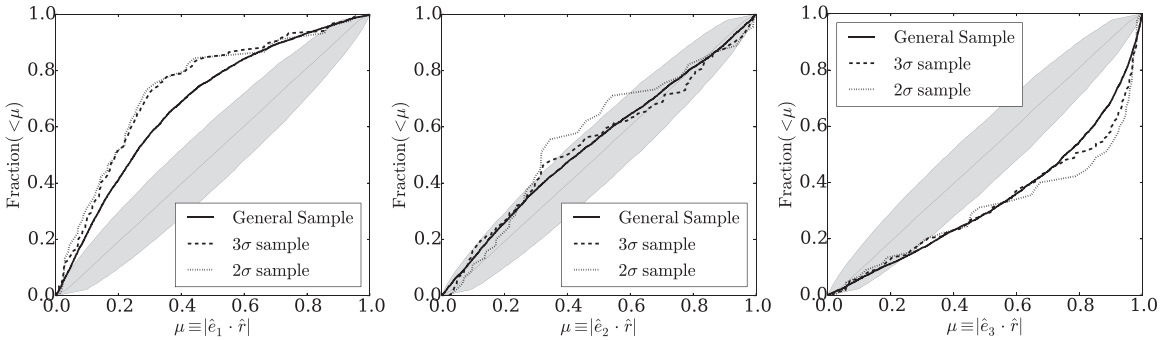

Figure 4. Cumulative distributions for the alignment between the vector linking the two halos in the pair, $\hat{r}$, and the three eigenvectors in the Tweb. The shaded region is the same as in Figure 3.

The left panel shows the overdensity dependence on pair mass. Higher-mass pairs are located in high-density regions. The 2σ and 3σ samples that have a narrower mass range, as shown in previous figure, are consequently located within a narrower range of overdensities $0.0 < \delta < 2.0$ peaking at $\delta \sim 1$. This is also consistent with the fact that these samples are mostly found in filaments and sheets.

The middle and right panels show web ellipticity and absolute prolateness dependence on mass. Again, we note that within the 2σ and 3σ mass range, the average ellipticity and prolateness does not differ significantly from the GS expectation. In the RS samples the pairs are located in a narrow range for ellipticities $0.1 < e < 1.0$ and absolute prolateness $|p| < 0.4$.

4.3. Alignments with the Cosmic Web

We now study different alignments of the LG with respect to the cosmic web. Figure 3 shows the alignment of the orbital angular momentum with the cosmic web, and Figure 4 repeats the same alignment plot, but using the pair orientation instead.

Orbital angular momentum. Figure 3 shows the cumulative distribution of $\mu \equiv \hat{e}_i \cdot \hat{n}$ for the three eigenvectors $i = 1, 2, 3$. Lines in each panel correspond to different samples. The straight line across the diagonal shows the expected result for vectors with randomly distributed directions.

There are two important features in Figure 3. First, the alignments themselves. There is a strong anti-alignment signature between $\hat{n}$ and the third eigenvector. With respect to the first and second eigenvector, the distribution is consistent with no alignment. Second, the alignment strength changes for the different samples. For the anti-alignment with $\hat{e}_3$, the signal strengthens as we move from the GS to the 3σ into the 2σ sample.

Quantitatively, the anti-alignment feature found with the $\hat{e}_3$ vector means that for the 2σ sample, $\sim$50% of pairs have $|\mu| < 0.2$ ($>78^\circ$ angle), and $\sim$75% of pairs have $|\mu| < 0.4$ ($>66^\circ$ angle). These signals do not change significantly in different environments, which has already been shown in different alignment studies with similar (Libeskind et al. 2013) or identical (Forero-Romero et al. 2014) web finding techniques as ours. In particular, these trends hold for pairs in filaments and walls. If we consider only pairs in filaments, we have that the pair orbital angular momentum tends to be perpendicular to the filament direction, in the case of sheets it tends to lie perpendicular to the sheet plane.

The alignment strength could be explained to a great extent by a total mass dependency. In Figure 5, we show the median of $\mu \equiv \hat{e}_i \cdot \hat{n}$ and $\mu \equiv \hat{e}_i \cdot \hat{r}$ in different mass bins. Lines show the median μ–mass relation for the three eigenvectors in the GS, dots represent the results for the 2σ–3σ samples. Around the total mass 1.5–$2.0 \times 10^{12}\ M_\odot$ in the RS samples, the median of μ from the 2σ and 3σ samples clearly differs from the GS results. However, the uncertainty level of the median for a small sample (indicated by the shaded region) makes this trend compatible with the values from the GS sample.

We also explored characteristics in the orbits that could be responsible for the strengthened alignment feature. We note that RS samples constrain the tangential velocity, and consequently pair orbits become more eccentric as we tighten pair constraints. For the GS sample, there is no tangential velocity constraint at all. We studied the relationship between orbit eccentricity and alignment computing for each halo pair in all of the samples with an approximate orbit eccentricity, assuming a two-body orbit with masses set as the virial masses and initial conditions given by the current velocity vector and separation. We found that selecting a subsample of GSs with the same eccentricity as 2σ–3σ samples does not increase in the alignment when compared with the full GS.

Radial vector. Figure 4 presents the results for the eigenvector alignments with respect to the vector connecting

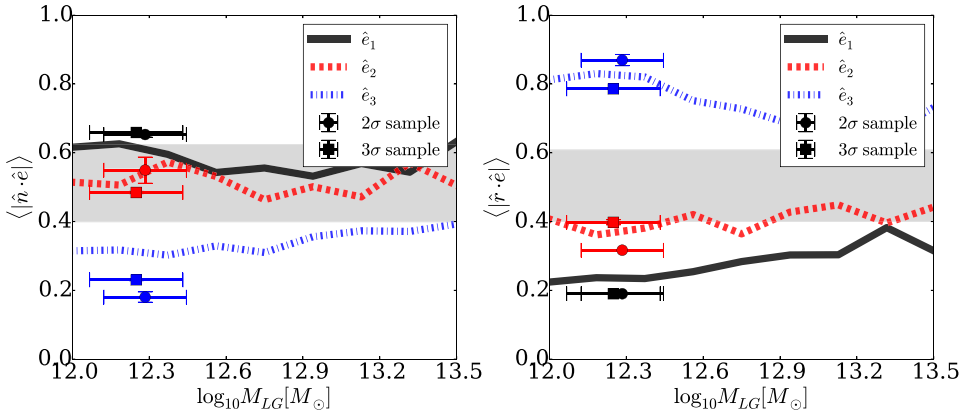

Figure 5. Mass dependency of the median value for the dot product between the normal/radial vector $\hat{n}/\hat{r}$ (left/right) and each one of the eigenvectors. The lines show trends for the general sample. The error bars in the 2σ and 3σ points correspond to jackknife estimates. The shaded region shows the expectation for a random distribution without any preferential alignment, it encloses the 5% and 95% percentiles of 10,000 flat distributions for μ generated with the same number of points as the 2σ sample.

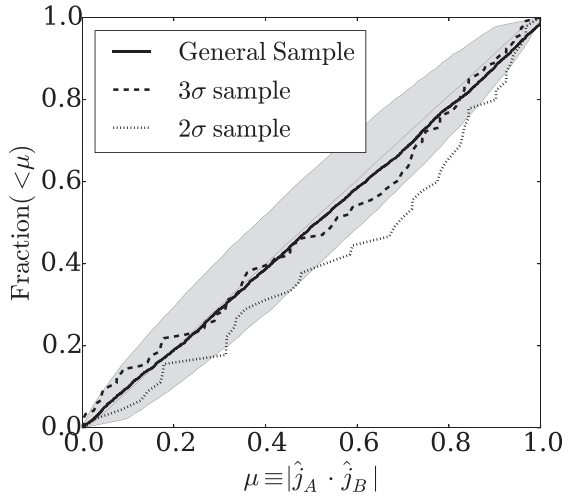

Figure 6. Alignment between the two angular momentum vectors of the two halos in the pair. The shaded region shows the expectation for a random distribution without a preferential alignment as it is described in Figure 5.

the two halos. In this case, we find that the vector $\hat{r}$ is strongly aligned along the direction defined by $\hat{e}_3$ and anti-aligned along $\hat{e}_1$; correspondingly, the signal along $\hat{e}_2$ is rather weak.

We also find a stronger signal as we move into more restrictive samples, though the signal from the GS is already very significant. Quantitatively, the alignment feature with $\hat{e}_3$ means that for the 2σ and 3σ samples, ~50% of the pairs have $|\mu| > 0.8$ (<36° angle) and ~25% of the pairs have $|\mu| > 0.95$ (<18° angle). Similar to the previous case of the $\hat{n}$ vector, the increasing strength of the $\hat{r}$ alignment can be explained to a great extent by a selection of mass.

Considering that the 2σ and 3σ samples correspond to pairs moving along the radial direction, we can say that the motion of the LG halos is mostly done along the $\hat{e}_3$ vectors. This is consistent with recent results that report a strong alignment of the halo's peculiar velocities along that direction (Forero-Romero et al. 2014).

Halo spin. We also explore the alignment of the angular momentum (spin) of each pair member $\hat{j}_A$ and $\hat{j}_B$ with each other, with the orbital angular momentum, and with the cosmic web.

Figure 6 shows the cumulative distribution of dot product between the angular momentum of both halos. We find a slight alignment of spin vectors for the 2σ sample with a median around $|\mu| \sim 0.7$ (45°), which is barely above the no-alignment expectation marked by the shaded region. Furthermore, we found no significant alignments with the pair orbital angular momentum nor with the cosmic web.

The absence of alignment for the spins is consistent with different studies of spin alignment that mark the range $10^{12}\ M_\odot$ as either a transition mass from alignment into anti-alignment or from no-alignment into alignment (Hahn et al. 2007; Aragón-Calvo et al. 2007; Zhang et al. 2009; Codis et al. 2012; Trowland et al. 2013; Libeskind et al. 2013; Forero-Romero et al. 2014). We refer the reader to Table 2 in Forero-Romero et al. (2014) for a review of the different results of spin alignment with the cosmic web in cosmological simulations. It seems that this transition is related to changes in the major merger rate as a dark matter halo approaches the $10^{12}\ M_\odot$ mass (Forero-Romero 2009; Codis et al. 2012).

In the LG, the angle between MW and M31 spin is ~60° ($|\mu| = 0.5$) and the angles between spins and orbital angular momentum are ~33° ($|\mu| = 0.83$) and ~76° ($|\mu| = 0.24$) for MW and M31, respectively (van der Marel et al. 2012a). This is consistent with our results that show no strong alignment.

5. DISCUSSION AND CONCLUSIONS

The mass range of the LG pairs is tightly correlated with the properties of the web in which they reside, as shown in Table 1 and Figure 1. This confirms that the local overdensity, the trace of the tidal tensor, is the dominant web parameter that defines the abundance and properties of halos (Lee & Shandarin 1998; Lemson & Kauffmann 1999; Sheth & Tormen 2004; Fakhouri & Ma 2009; Alonso et al. 2014). Other quantities derived from the tidal tensor play secondary roles in defining properties such as formation history.

In our case, the fact that the preferred LG total mass is around $1\text{–}4 \times 10^{12}\ M_\odot$ implies that the preferred environments are filaments and sheets with overdensities close to the average value. Correspondingly, the values for the ellipticity and prolateness are also well defined for the LG pairs given its correlation with the total mass.

We conclude that the typical LG environment and its characteristics are robust results depending mostly on the LG total mass.

The alignments with the cosmic web also have a mass dependency. Although they seem to be stronger once the

kinematic constraints are imposed on the GS pairs, the results are consistent with the simple mass cut on the GS sample. There is a clear anti-alignment between the third eigenvector and the orbital angular momentum vector, meaning that this vector is perpendicular to both filaments and sheets. We also found that the vector joining the LG halos are aligned with the third eigenvector. This means that the pair is aligned with the filaments and lies on the sheets, and its motion is done along these directions.

These alignment features are in agreement with the scenario that pairs created in situ or falling into a filament/wall align their orbits with the large-scale structure in a relaxation process where pair members tend to move along the slowest collapsing directions.

How can we relate these alignments to the observed LG? To evaluate this point, we use observational information for the satellite distribution around the LG galaxies. The MW satellites are located at high galactic latitudes forming a planar structure that forms an angle of 42°–52° ($\mu = 0.6$–0.7) with the vector joining the MW and M31; while the M31 satellites are on a plane that lies on the same vector (Pawlowski et al. 2013; Shaya & Tully 2013).

Most ΛCDM studies find that sub-structure infall direction is done along $\hat{e}_3$ (the direction of filaments; Zentner et al. 2005; Bailin et al. 2008) or almost over the plane defined by the $\hat{e}_2$ and $\hat{e}_3$ (Libeskind et al. 2014).

Taking these three points together (the alignment of MW–M31 along $\hat{e}_3$, the observed satellite alignments and the preferential infall along $\hat{e}_3$), we note that the M31 plane of satellites is completely consistent with the average alignment picture that we have described. However, the plane defined by the MW satellites should also be close to parallel with respect to the vector joining MW and M31 and the plane of M31 satellites. Instead, this plane has $\mu = 0.6$–0.7 with respect to these directions. Therefore, we suggest that the spatial location of MW satellites raises a potential contradiction with the average expectations from ΛCDM, a point that has been mentioned before (Pawlowski et al. 2012, 2014).

This apparent contradiction can be solved if one considers that the subhalo infall properties depend on the environment at *the merger time*, while the alignments for yet unvirialized pairs such as the dominant galaxies in the LG depend on the current state of the cosmic web. This also explains the absence of a strong alignment with halo spin, because it reflects past configurations of the web, not the current one. From this perspective, a joint consideration of the alignments between the dominant halos in the LG and their satellites, which also feature strong signals (Kroupa et al. 2005; Pawlowski et al. 2013; Shaya & Tully 2013), should inform us of the structural evolution of the cosmic web around the LG.

Our results raise the need to observationally constrain the alignments of LG pairs with their cosmic web environment. To this end, one could use mass reconstructions from large surveys (Wang et al. 2009; Muñoz-Cuartas et al. 2011; Nuza et al. 2014; Wang et al. 2014) or filament finders (González & Padilla 2010; Sousbie 2011) to select an LG sample to quantify the alignments with the surrounding filamentary structure. This would allow not only a direct quantification of how common the LG alignments are but also provide a new test of ΛCDM.

J.E.F.R. was supported by an FAPA grant by Vicerrectoría de Investigaciones at Universidad de los Andes in Bogotá, Colombia. R.E.G. was supported by Proyecto Financiamiento Basal PFB-06 "Centro de Astronomia y Tecnologias Afines" and Proyecto Comité Mixto ESO 3312-013-82. The Geryon cluster at the Centro de Astro-Ingenieria UC was extensively used for the calculations performed in this paper. The Anillo ACT-86, FONDEQUIP AIC-57, and QUIMAL 130008 provided funding for several improvements to the Geryon cluster. The authors thank Andrey Kravtsov and Nelson Padilla for their useful comments; Yehuda Hoffman for insightful conversations on the subject of the LG and the Cosmic Web; and the referee Noam Libeskind that helped us to clarify and strengthen the results presented in the paper.

REFERENCES

Alonso, D., Eardley, E., & Peacock, J. A. 2014, arXiv:1406.4159
Aragon-Calvo, M. A., Silk, J., & Szalay, A. S. 2011, MNRAS, 415, L16
Aragón-Calvo, M. A., van de Weygaert, R., Jones, B. J. T., & van der Hulst, J. M. 2007, ApJL, 655, L5
Bailin, J., Power, C., Norberg, P., Zaritsky, D., & Gibson, B. K. 2008, MNRAS, 390, 1133
Cautun, M., van de Weygaert, R., Jones, B. J. T., & Frenk, C. S. 2014, MNRAS, 441, 2923
Codis, S., Pichon, C., Devriendt, J., et al. 2012, MNRAS, 427, 3320
Courtois, H. M., Pomarède, D., Tully, R. B., Hoffman, Y., & Courtois, D. 2013, AJ, 146, 69
Cox, T. J., & Loeb, A. 2008, MNRAS, 386, 461
Fakhouri, O., & Ma, C.-P. 2009, MNRAS, 394, 1825
Forero-Romero, J. E. 2009, MNRAS, 399, 762
Forero-Romero, J. E., Contreras, S., & Padilla, N. 2014, MNRAS, 443, 1090
Forero-Romero, J. E., Hoffman, Y., Bustamante, S., Gottlöber, S., & Yepes, G. 2013, ApJL, 767, L5
Forero-Romero, J. E., Hoffman, Y., Gottlöber, S., Klypin, A., & Yepes, G. 2009, MNRAS, 396, 1815
Forero-Romero, J. E., Hoffman, Y., Yepes, G., et al. 2011, MNRAS, 417, 1434
González, R. E., Kravtsov, A. V., & Gnedin, N. Y. 2013, ApJ, 770, 96
González, R. E., Kravtsov, A. V., & Gnedin, N. Y. 2014, ApJ, 793, 91
González, R. E., & Padilla, N. D. 2010, MNRAS, 407, 1449
Hahn, O., Carollo, C. M., Porciani, C., & Dekel, A. 2007, MNRAS, 381, 41
Hinshaw, G., Larson, D., Komatsu, E., et al. 2013, ApJS, 208, 19
Karachentsev, I. D. 2005, AJ, 129, 178
Klypin, A., Hoffman, Y., Kravtsov, A. V., & Gottlöber, S. 2003, ApJ, 596, 19
Klypin, A., & Holtzman, J. 1997, arXiv:astro-ph/971227
Klypin, A. A., Trujillo-Gomez, S., & Primack, J. 2011, ApJ, 740, 102
Kroupa, P., Theis, C., & Boily, C. M. 2005, A&A, 431, 517
Lee, J., & Shandarin, S. F. 1998, ApJ, 500, 14
Lemson, G., & Kauffmann, G. 1999, MNRAS, 302, 111
Li, Y.-S., & White, S. D. M. 2008, MNRAS, 384, 1459
Libeskind, N. I., Hoffman, Y., Forero-Romero, J., et al. 2013, MNRAS, 428, 2489
Libeskind, N. I., Knebe, A., Hoffman, Y., & Gottlöber, S. 2014, MNRAS, 443, 1274
Mei, S., Blakeslee, J. P., Côté, P., et al. 2007, ApJ, 655, 144
Muñoz-Cuartas, J. C., Müller, V., & Forero-Romero, J. E. 2011, MNRAS, 417, 1303
Nuza, S. E., Kitaura, F.-S., Heß, S., Libeskind, N. I., & Müller, V. 2014, MNRAS, 445, 988
Pawlowski, M. S., Famaey, B., Jerjen, H., et al. 2014, MNRAS, 442, 2362
Pawlowski, M. S., Kroupa, P., Angus, G., et al. 2012, MNRAS, 424, 80
Pawlowski, M. S., Kroupa, P., & Jerjen, H. 2013, MNRAS, 435, 1928
Riebe, K., Partl, A. M., Enke, H., et al. 2013, AN, 334, 691
Sandage, A., & Tammann, G. A. 1975, ApJ, 196, 313
Shaya, E. J., & Tully, R. B. 2013, MNRAS, 436, 2096
Sheth, R. K., & Tormen, G. 2004, MNRAS, 350, 1385
Sohn, S. T., Anderson, J., & van der Marel, R. P. 2012, ApJ, 753, 7
Sousbie, T. 2011, MNRAS, 414, 350
Trowland, H. E., Lewis, G. F., & Bland-Hawthorn, J. 2013, ApJ, 762, 72
van der Marel, R. P., Besla, G., Cox, T. J., Sohn, S. T., & Anderson, J. 2012a, ApJ, 753, 9
van der Marel, R. P., Fardal, M., Besla, G., et al. 2012b, ApJ, 753, 8
Wang, H., Mo, H. J., Jing, Y. P., et al. 2009, MNRAS, 394, 398
Wang, H., Mo, H. J., Yang, X., Jing, Y. P., & Lin, W. P. 2014, ApJ, 794, 94
Zentner, A. R., Kravtsov, A. V., Gnedin, O. Y., & Klypin, A. A. 2005, ApJ, 629, 219
Zhang, Y., Yang, X., Faltenbacher, A., et al. 2009, ApJ, 706, 747